

## Chapter 4

### Apparatus

In this chapter, I will describe the apparatus used to realize the interactions discussed in the last Chapter (the ion trapping apparatus was discussed in Ch. 2). First, I will discuss the laser and optical systems used to cool and manipulate the ion's motional state. Then I will describe the digital logic and rf control used to switch the laser beams on and off and control their frequency. The experiment was a fluid object, constantly changing and evolving. In order to describe it, I have had to choose one particular configuration. However, this setup was generically the same as any of the other incarnations of the laser systems.

#### 4.1 Optics

The optical setup of the experiment was divided into three sets of beam lines: (i) the beams used for optical pumping, Doppler cooling and driving the cycling transition, (ii) the “repumper,” used to clean out the  $2s\ 2^S_{1/2}F = 2, m_F = -1$  level, and (iii) the Raman beams. The orientation of these beam lines with respect to the vacuum envelope of the trap is shown in Fig. 4.1. For each of these beam lines, the wavelength of the light at the ion was  $\approx 313$  nm. This light was created by frequency-doubling light from a 626 nm dye laser (the dye was Kiton Red), pumped by green light from an argon-ion laser. The argon-ion laser was a Spectra Physics Model 2030, which was usually run

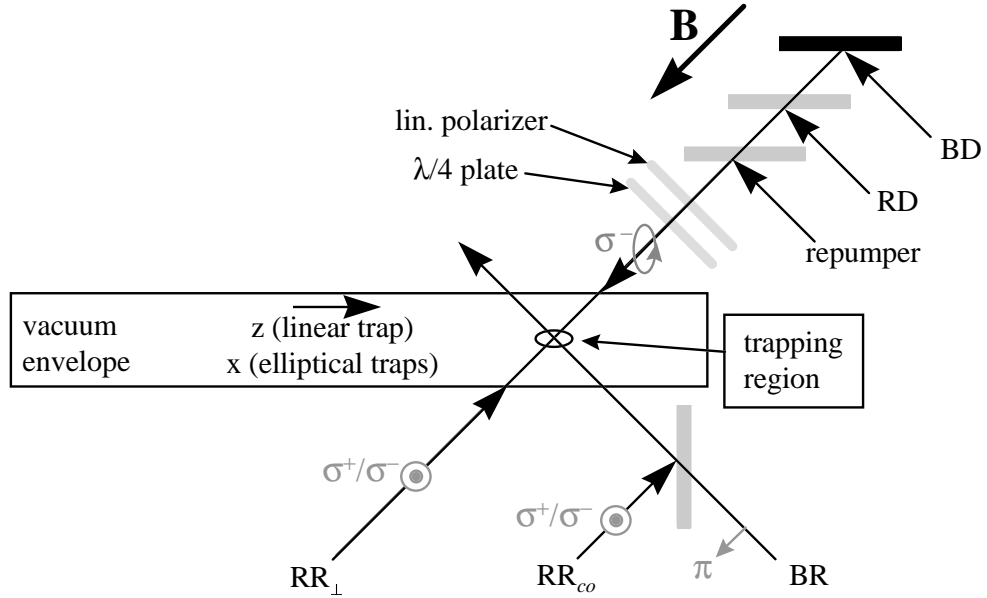


Figure 4.1: Laser beam geometry. The long axis of the vacuum envelope was parallel to the  $x$ -axis for the elliptical microtraps, and parallel to the  $z$ -axis for the micromachined linear ion trap. The Blue Doppler, Red Doppler and repumper beams entered the trap through the same window. The Red Raman  $\perp$  beam entered through the opposite window. The Blue Raman beam and the Red Raman  $co$  beam entered at  $90^\circ$  to the Red Raman  $\perp$  beam. The resonant beams were polarized  $\sigma^-$ , Blue Raman was  $\pi$ -polarized,  $RR_{co}$  was polarized  $(\sigma^+ + \sigma^-)/2^{1/2}$ , and  $RR_{\perp}$ 's polarization was selected as discussed in Ch. 6.2.1: usually, its polarization was  $(\sigma^+ + \sigma^-)/2^{1/2}$  as well.

with an output power of  $\approx 16.8$  W. This light was then split three ways by optical beam splitters: roughly 5.6 W was sent to each of the dye lasers.

The argon-ion laser and all the 626 nm optics associated with the dye lasers and their locking systems were on one optical table (the “red table”). The frequency doubling, the 313 nm optics and optical switches, and the ion trap were on a second optical table (the “UV table”). The 626 nm light was passed to this table through fibre optics.

#### 4.1.1 Resonant Beam Lines: the Doppler and Repumper Beams

A schematic diagram of the resonant beam lines (the Doppler and repumper lines) is shown in Fig. 4.2. There were two “Doppler” beams: the Blue and Red Doppler. The names arose from the frequencies of the two beams: since the Blue Doppler connected  $|\downarrow\rangle$  with the  $2p\ ^2P_{3/2}$  level, it was of higher frequency than the Red Doppler, which connected  $|\uparrow\rangle$  with the same state. Blue Doppler drove the cycling transition used for state detection (see Sec. 3.1), and provided laser cooling. Red Doppler was also turned on during laser cooling and, in conjunction with the repumper laser, provided optical pumping.

The Doppler beams were produced by a Coherent 699 dye laser circulating Kiton Red (at a pressure of 40-55 psi). The conversion efficiency from the green pump light to 626 nm output was approximately 10% (depending on the age of the dye and the state of the laser cavity). So, with 5.6 W of green pump light, the laser produced up to 600 mW of output light. The 699 has an internal cavity assembly consisting of a thin and thick etalon, and a Brewster-angle plate used to scan the laser over large frequency ranges (in principle, up to tens of GigaHertz). The laser was modulation-locked to the maximum of the thick etalon transmission. Frequency stability was provided by locking to an external, stable reference cavity (a “side-lock” to the side of the external cavity’s transmission). The error signal derived from the reference cavity was fed back to the Brewster-angle plate and to a piezo-electric transducer which supported one of the laser cavity mirrors. By tuning the laser to the side of the transmission curve of an external cavity, we could determine that the 699 typically exhibited a linewidth of 1-4 MHz when locked up.

A portion of the 699’s output light was split off by a beam splitter and sent to diagnostics. These diagnostics consisted of a Burleigh Model #SA-PLUS-200-B1 spectrum analyzer (2 GHz free spectral range), a travelling-cart wavemeter [97, 98], and

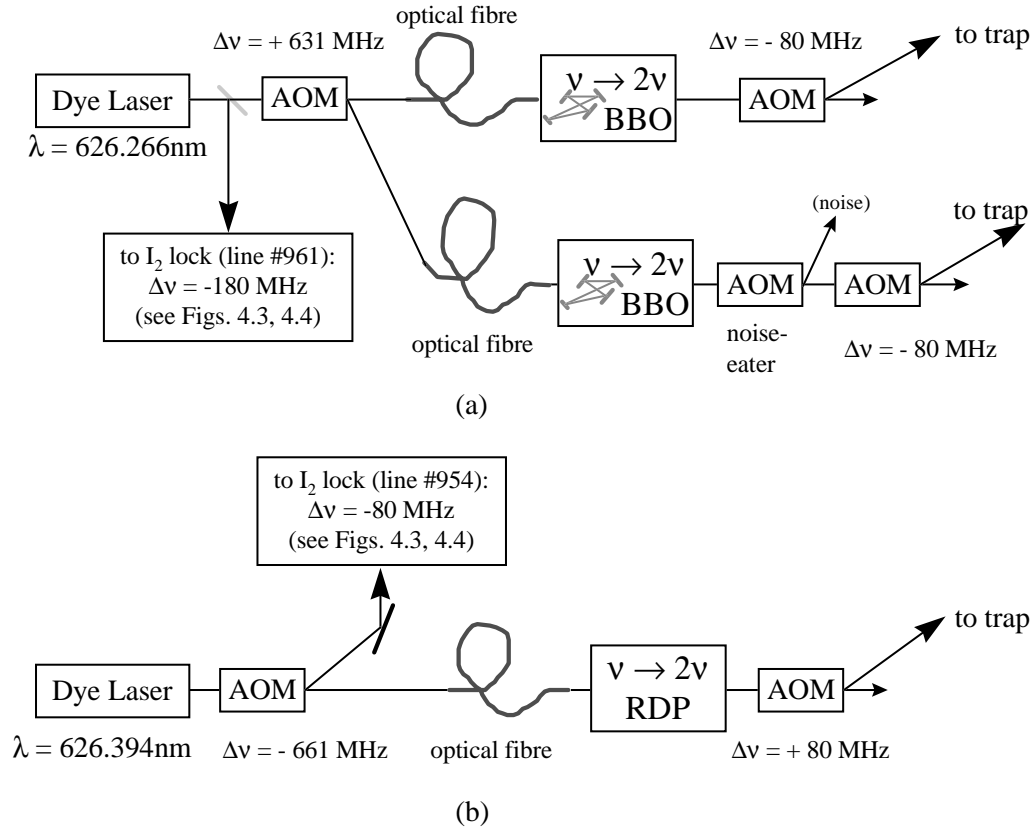


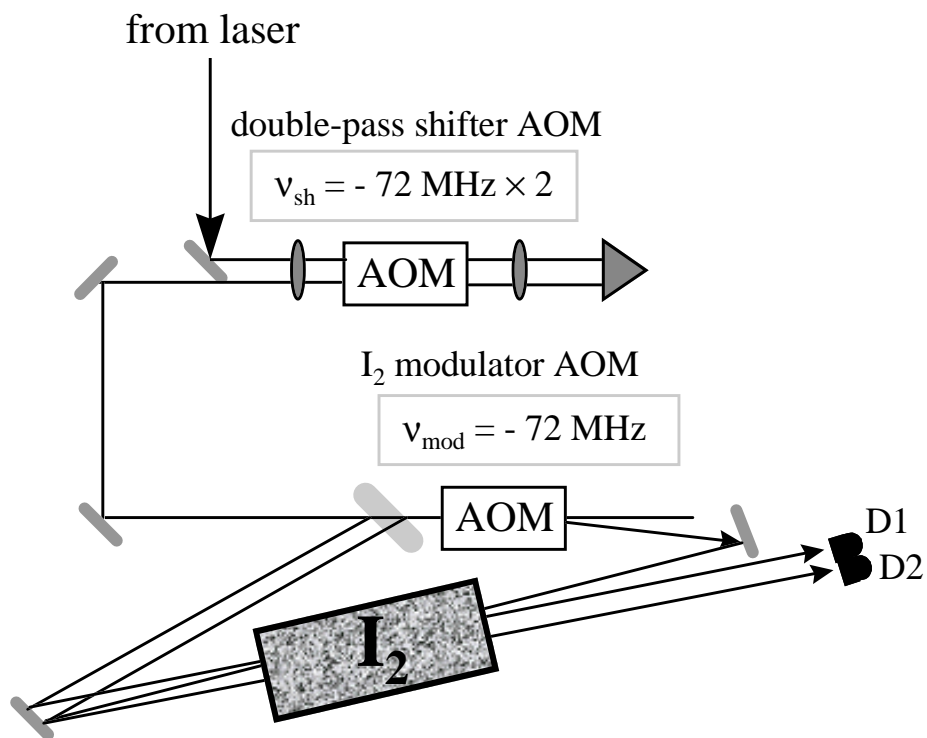
Figure 4.2: Resonant beam lines: Doppler (a) and repumper (b). The Doppler beams were derived from a Coherent 699 dye laser. The 1.26 GHz hyperfine and Zeeman splitting between Red and Blue Doppler was achieved with a 631 MHz AOM in the red (i.e. at 626 nm). The frequencies of the beams were doubled in a BBO ( $\beta$ -barium borate) crystal inside a double-ring optical resonator structure. In the UV (at 313 nm), the frequency difference between the two beams became 1.26 GHz. The beams were turned on and off with two more “switch” AOMs. The BBO rings and the UV optics were on a separate optical table from the dye laser, its Ar-ion pump laser, and the laser diagnostics. Light at 626 nm passed between the two tables through a single-mode optical fibre. The repumper beam was derived from a home-built dye laser. This beam line was generically equivalent to the Doppler beam lines, except that the frequency doubling was performed by single-passing the red light through a cooled RDP crystal.

an  $I_2$  saturated absorption spectrometer [99]. The spectral features of the iodine provided a stable reference to which to lock the laser at long times. Details of the setup are shown in figure 4.3(a). The laser light first passed through a double-pass AOM, where it picked up a frequency offset (from the laser output) of  $\Delta\nu = -2 \times 72 \text{ MHz} = -144 \text{ MHz}$ . This double-pass configuration allowed us to change the frequency offset between the laser light and the iodine lock without causing appreciable beam steering. From there, the light passed through a thick beam splitter (approximately 4% reflectance per face), which produced the weak probe and reference beams for the saturated spectroscopy. The transmitted beam passed through another AOM: this AOM produced a frequency shift of  $\Delta\nu = -72 \text{ MHz}$  in the pump beam. The frequency of the rf driving this AOM was modulated at  $\approx 3 \text{ kHz}$  in order to allow lock-in detection of the iodine fluorescence.<sup>1</sup> The modulation depth was on the order of the linewidth of the iodine features ( $\approx 5 - 10 \text{ MHz}$ ).

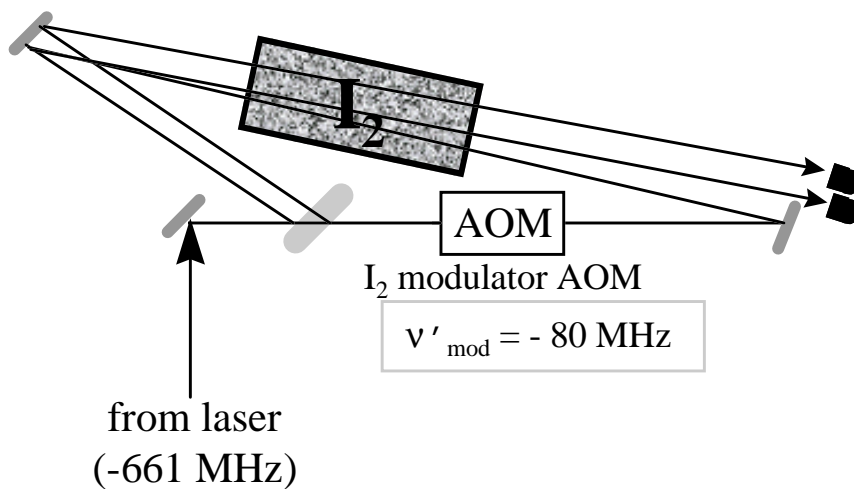
As usual in saturated absorption spectroscopy [99], the strong pump beam saturated the  $I_2$  population with which it was resonant. This depleted the absorption signal of the weak (counter-propagating) probe beam in the velocity class of  $I_2$  which was simultaneously in resonance with the pump and probe beams. Subtraction of the reference beam signal from the probe beam signal removed the background absorption profile of the probe beam (and also reduced the effects of laser intensity fluctuations), leaving only the narrow, Doppler-free, saturated-absorption dip. The pump beam was frequency-modulated at 30 kHz to move the saturated-absorption signal away from DC, using standard phase-sensitive detection techniques [100]. The probe and reference beams were detected and subtracted in a New-Focus Nirvana auto-balanced photodiode-pair detector, and the output was sent to a lock-in amplifier, which fed back into the 699 control box lock circuitry.

---

<sup>1</sup> Note that, if the beam had been modulated *before* the beam splitter, then the reference beam would have had 30 kHz FM on it. If the amplitude of this beam fluctuated, the fluctuations then would have passed through the phase-sensitive detection to the lock signal.



(a)



(b)

Figure 4.3: Schematic of the saturated absorption spectrometers used to lock the Doppler (a) and repumper (b) lasers to iodine. The frequencies driving the various AOMs are indicated. Note that the “modulation” AOM frequency shift was effectively half the frequency driving the AOM. The beam which went to the iodine lock from the repumper laser was first down-shifted by 661 MHz.

The 699 was locked to hyperfine feature (a) of line # 961 of the “Iodine atlas” [101]. See Fig. 4.4(a) for a spectrum of this iodine line. Feature a lies at the blue-most edge of line # 961: thus, if the laser (on resonance with the  ${}^9\text{Be}^+, |\downarrow\rangle \rightarrow |2p\ ^2P_{3/2}\rangle$ ) transition jumped out of lock, it would not re-lock to the blue of resonance (which would cause heating). There was no lock point to the blue of Feature (a).

From Figs. 4.2 and 4.3(a), we can determine the relationship between the frequency  $\nu_{I_2}$  of Feature a of line # 961 of  $\text{I}_2$  and the  $|\uparrow\rangle \rightarrow |2p\ ^2P_{3/2}\rangle$  resonance <sup>2</sup> frequency  $\nu_{Be}$  of the ion. First note that, in order for both the pump and probe beams to be in resonance with the same velocity class of the  $\text{I}_2$  sample, we must have

$$\begin{array}{ccc} \text{probe beam} & & \text{pump beam} \\ \nu_L - 2\nu_{sh} - \nu_D & = & \nu_L - 2\nu_{sh} - \nu_{mod} + \nu_D. \end{array} \quad (4.1)$$

Here,  $\nu_L$  is the frequency of the laser’s output,  $\nu_{sh} = 72$  MHz is the frequency driving the double-pass AOM,  $\nu_{mod} = 72$  MHz is the frequency driving the pump-beam modulation AOM, and  $\nu_D$  is the magnitude of the Doppler shift of the selected velocity class. Equation (4.1) implies that

$$\nu_D = \frac{1}{2}\nu_{mod}. \quad (4.2)$$

Finally, we have

$$\begin{aligned} \nu_{Be} &= 2(\nu_{I_2} + 2\nu_{sh} + \nu_{mod} + \nu_D) - 80 \text{ MHz} \\ &= 2\left(\nu_{I_2} + 2\nu_{sh} + \frac{1}{2}\nu_{mod}\right) - 80 \text{ MHz} \\ &= 2\nu_{I_2} + 280 \text{ MHz} . \end{aligned} \quad (4.3)$$

The main part of the Doppler laser’s power passed through a high-frequency AOM which was driven at 631 MHz (half the  ${}^9\text{Be}^+$  hyperfine splitting, plus Zeeman shifts). The undeflected beam produced the Red Doppler beam when doubled, while

---

<sup>2</sup> Recall that  $|\uparrow\rangle \equiv |2s\ ^2S_{1/2}, F = 1, m_F = -1\rangle$ .

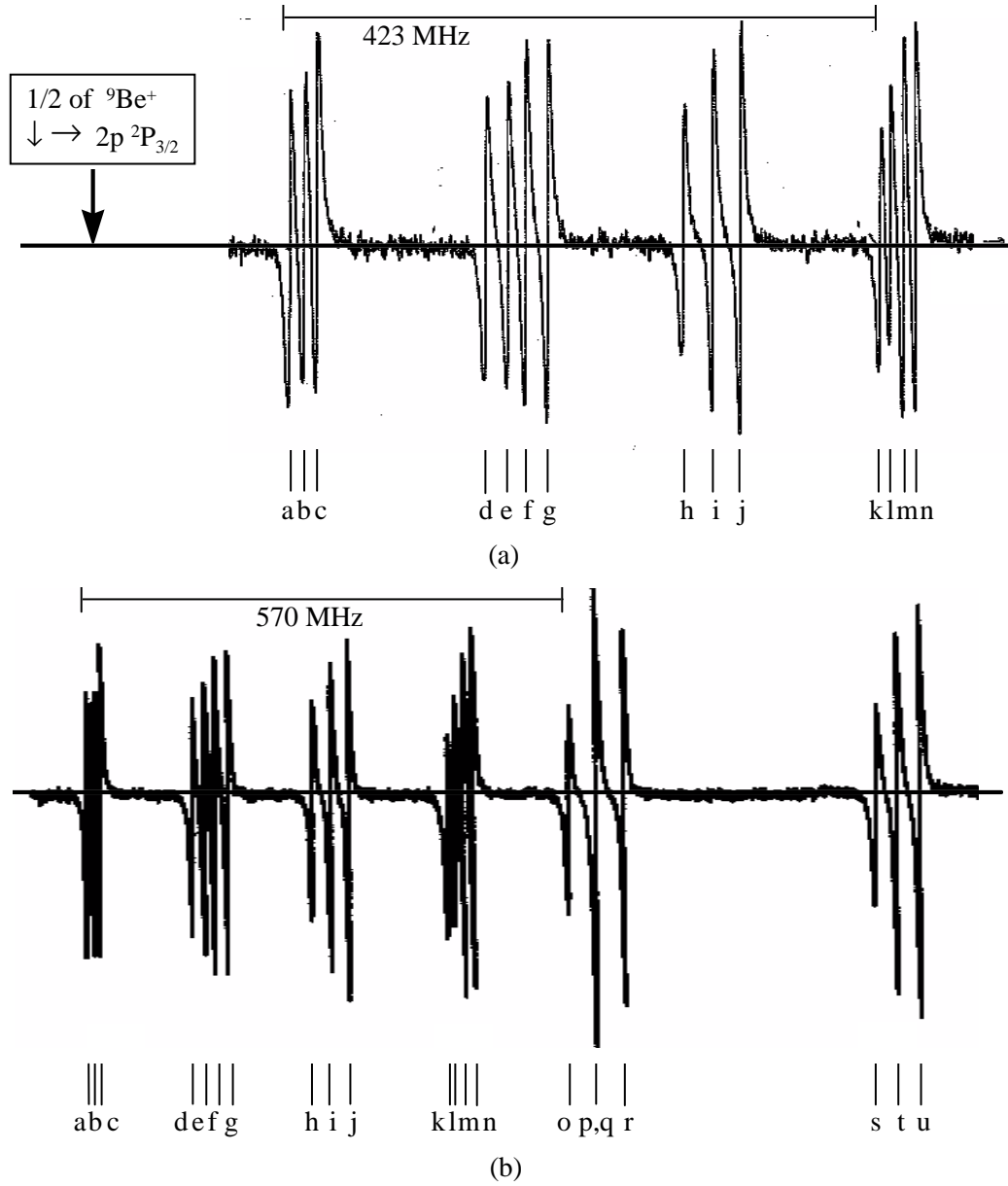


Figure 4.4: (a) Portion of I<sub>2</sub> line # 961, as traced out by saturated absorption spectroscopy. The line is the result of the phase-sensitive detection signal of the photodiode current difference between the probe and reference beams, as described in the text. The Doppler laser was locked to Feature (a). Features (o) through (u) are not shown on this trace: they lie to the right of Feature (n), which is towards lower frequencies. The relative position of the <sup>9</sup>Be<sup>+</sup>, |↑⟩ → |2p <sup>2</sup>P<sub>3/2</sub>⟩ resonance (after frequency doubling) is indicated by the arrow. From the text, the 626 nm light which was doubled to be on resonance with this transition lay 140 MHz to the blue of Feature (a). (b) Complete trace of I<sub>2</sub> line # 954. The repumper laser was locked to Feature (a) of this line. The 626 nm light which, when frequency doubled, drove the |F = 2, m<sub>F</sub> = -1⟩ → |2p <sup>2</sup>P<sub>1/2</sub>⟩ transition, was 681 MHz to the blue of this feature.

the (positive) first-order diffracted beam produced the Blue Doppler. These two beams were then coupled from the “red” table to the “UV” table through single-mode fibres. The fibres were a convenient way to pass the light from one table to the other, since they allowed us to change the alignment of the “red” optics without affecting the doubling ring or UV optics alignment.<sup>3</sup>

Frequency doubling of the 626 nm Doppler-line light occurred in a BBO crystal which was enclosed in a double-ring cavity (see Fig. 4.5). The two rings shared three of the four mirrors which comprised their respective cavities, as well as the BBO crystal in which the frequency-doubling took place, and the UV output-coupler. The mirrors which the two rings did not share were mounted on piezo-electric transducers, which allowed feedback of an error signal to lock the cavity. Sharing one BBO crystal between the two beams was a convenient way to maximize the use of the BBO crystal.

As Fig. 4.5 indicates, each ring was in a bow-tie configuration. The long side of the bow-tie was 15 cm in length, whereas the short side was 10.6 cm long. The other relevant dimensions are shown in Fig. 4.5. Two of the mirrors were high-reflectance ( $R > 99.9\%$ ), 10 cm radius of curvature mirrors. The piezo-mounted mirror was a high-reflectance ( $R > 99.9\%$ ) flat. The final mirror, which served as the input coupler, was a 98.5% reflectance flat. Coupling into the cavity was achieved through two telescopes, each of which consisted of two, 10 cm lenses. The polarization of the 626 nm light inside the cavity was in the plane of the ring (horizontal). The cavity had a finesse of  $\approx 200$  and a free spectral range of approximately 0.5 GHz. The power build-up factor was measured to be  $\approx 75$ . The cavities were locked on resonance by monitoring the polarization of the 626 nm light reflected off the input coupler, according to the scheme of Hänsch and Couillaud [102], and feeding the resultant error signal back to the piezo-mounted cavity mirrors.

---

<sup>3</sup> Of course, changing the red alignment necessitated realignment of the fibres’ input couplers.

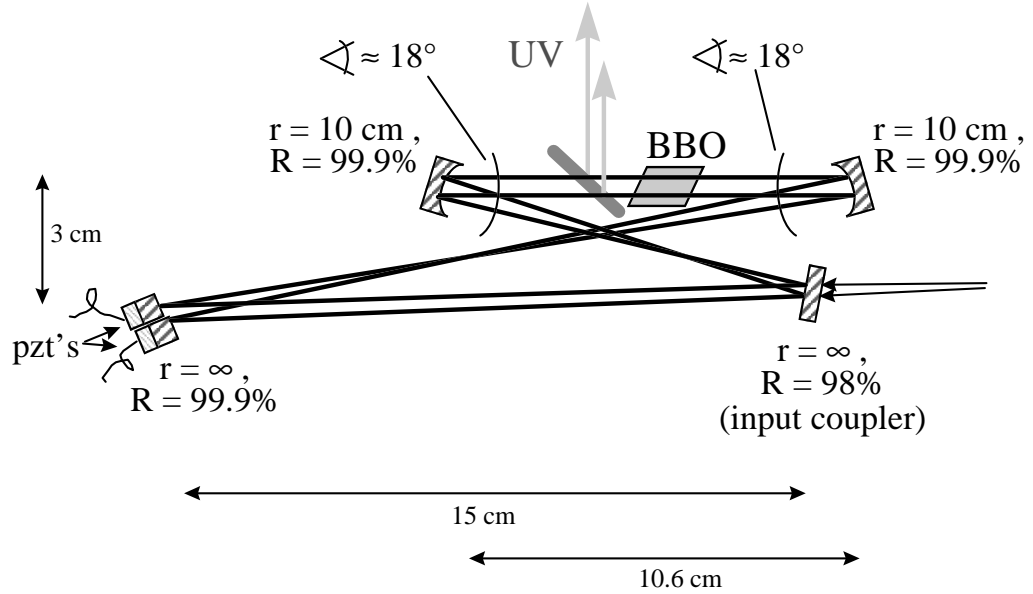


Figure 4.5: Resonant power build-up ring cavities for frequency doubling 626 nm to 313 nm. With 220 mW of 626 nm light coupled into one of the cavities, approximately 15-20 mW of 313 nm light was produced. Type II phase matching was used.

The BBO crystal was approximately 6 mm (length) by 4 mm by 4 mm. It lay in the short section of the cavity bow-tie, and its front and rear facets were cut at Brewster's angle with respect to the horizontally polarized, 626 nm light. The two fundamental beams (for Blue and Red Doppler) passed through the BBO crystal parallel. Second-harmonic generation was achieved through angle-tuned, Type II phase matching, and the crystal was cut so as to satisfy the phase-matching condition. The relevant BBO optical properties at 626 nm are listed in Table 4.1. From the nonlinear coefficient  $d_{20}$  and the beam characteristics, we would expect a conversion efficiency [103]  $\eta_{nl} = \frac{P^{2\omega}}{[P^\omega]^2} \approx 1 \times 10^{-4}/\text{W}$  (where the powers are measured in Watts). In practice, with 200 mW of power entering the cavity, 10 mW of UV was produced (corresponding to an inter-cavity doubling efficiency of  $\eta \approx 5 \times 10^{-5}/\text{W}$ ). The UV was coupled out of the cavity with a dichroic beam splitter, which reflected the 313 nm light out of the ring while presenting little loss ( $< 0.5\%$ ) to the 626 nm light.

Table 4.1: Optical characteristics of  $\beta$ -barium borate (BBO) at 626 nm and room temperature [104]. The second-harmonic generation scheme uses 626 nm (ordinary ray) + 626 nm (extraordinary ray) = 313.0 nm (extraordinary ray).

property	value
refractive index (o,e)	1.66747, 1.61568
$d_{eff}$	1.77 pm/V
Phase matching angle	38.4°
Walk off (o,e)	0.00 mrad, 72.89 mrad

The UV light (at 313 nm) passed from the cavity to an AOM (Intra-Action Model #ASM-802B8.<sup>4</sup> The negative first order diffracted spot (with a frequency shift  $\Delta\nu = -80$  MHz) was then sent to the trap. Thus, by turning the rf which drove the AOM on and off, we could turn on and off the UV at the trap. Details of the rf switching will be discussed in Sec. 4.2.1. The conversion efficiency of this switch AOM was  $\approx 80\%$  when driven with  $\approx 2$  W of rf.

Since the Blue Doppler beam drove the cycling transition, which was our only observable in the experiment, it was imperative that this beam have stable intensity. For this reason, the Blue Doppler beam passed through a “noise-eater” AOM before the switch AOM. Blue Doppler’s intensity was monitored by fast photodiodes after the frequency-doubling ring, and the results were accumulated on a fast integrator, which derived an error signal. This error signal was mixed with the rf driving the noise-eater AOM in order to control the light intensity: intensity fluctuations were shunted into the AOMs first-order deflected beam. The undeflected beam thus exhibited reduced amplitude fluctuations (up to  $\approx 100$  kHz), and this beam was passed on to the Blue Doppler switch AOM. The noise-eater circuitry did not have a sample-and-hold capability, and so had to be placed before of the switching AOM.

From the switch AOMs, the light passed through a linear polarizer and then through a quarter-wave plate. This produced pure circularly polarized light so that the

---

<sup>4</sup> This was the same model as all the other UV AOMs.

ion could be illuminated by pure  $\sigma^-$  light.<sup>5</sup> The quantization axis for the ion was set with a magnetic field coil whose axis of symmetry was roughly coincident with the laser beam propagation direction. The coil was outside the vacuum envelope, about 15 cm in diameter, and about 7.5 cm from the ion trap, producing a field of about eight Gauss at the location of the ion with several Ampères of current passing through the coil. Fine adjustments of the quantization direction and nulling out of external fields (such as that due to the Earth’s magnetic field) were accomplished with two similar coil coils at right angles to the first and an equal distance from the trap.

The UV was focussed onto the ion with a 10 cm focal length, UV lens, which was external to the glass vacuum envelope. This lens was mounted on an XYZ-translator. As indicated in Fig. 4.1, the Blue Doppler beam was combined with the Red Doppler on a 50-50 beam splitter. These two beams were then combined with the repumper (the weakest of the resonant beams) on another 50-50 beam splitter before passing through the polarizer, quarter-wave plate, the lens, the vacuum window, and into the trapping region.

The repumper beam line was quite similar in its features to the Doppler beam line. The main differences were in the dye laser and in the crystal used for frequency doubling. The dye laser used to produce 626 nm light for the repumper beam was a Jim Bergquist-designed, “home-built” ring laser. The ring cavity had a free spectral range of 100 MHz. Single direction lasing was ensured by an optical diode in the ring cavity, and frequency selectivity was achieved by a manually-tuned birefringent filter (200 GHz free spectral range),<sup>6</sup> a galvanometer-driven thin etalon (20 GHz free spectral range) and a thick etalon assembly (1.6 GHz free spectral range).<sup>7</sup> Fine tuning was accomplished with a piezo-mounted mirror which was one of the ring cavity mirrors. The laser was

---

<sup>5</sup> A method for peaking up the polarization of the light is discussed in Appendix A.

<sup>6</sup> This birefringent filter assembly was purchased from Coherent Radiation, Inc., and was the assembly used in their 699

<sup>7</sup> Again, this thick etalon assembly was the same as used in Coherent’s Model 699

kept on-mode with a dither-lock feeding back to the thick etalon — this kept the laser at maximum output intensity. Short-term frequency stability was ensured by locking the laser to an external Invar cavity (750 MHz free spectral range) using a Hänsch-Couillaud scheme to feed back to one of the ring-cavity mirrors. (This is in contrast to the Coherent 699, which uses a side-lock technique.) Unlike the 699 laser, the home-built laser did not have a Brewster-angle plate; however, it was still possible to scan the laser frequency by approximately 2 GHz. With 5.6 W of pump light, the laser typically put out between 650 and 750 mW, depending on the age of the dye and the day-to-day condition of the laser cavity. With the described locking scheme, the linewidth of the laser varied between 50 and 200 kHz, again depending on the day-to-day condition of the laser cavity.

As with the Doppler laser, a small portion of the output of this laser was split off with a beam splitter, and sent to the spectrum analyzer and travelling-cart wavemeter. The rest of the light passed through a high-frequency AOM: the undeflected beam was coupled through a single-mode optical fibre to the UV table, whereas approximately 30 mW in the negative first-order diffracted beam was sent off to a saturated-absorption iodine spectrometer.

This iodine setup, which is shown in Fig. 4.3(b), was used for long-term frequency stability of the repumper. The apparatus was very similar to that described above for the  $I_2$  lock of the 699 dye laser, except that the double-pass AOM was absent in the repumper beam line. The error signal from the lock-in amplifier was fed back to the piezo-mounted cavity mirror of the laser ring cavity. The high-frequency splitter AOM which deflected the beam into the  $I_2$  set up was driven with 661 MHz rf, the modulating AOM shifted the pump beam by  $\Delta\nu = -80 \text{ MHz} = \nu'_{mod}$ , and, as Fig. 4.2 shows, the UV switch AOM added a frequency shift of  $\Delta\nu = +80 \text{ MHz}$  to the UV (instead of the -80 MHz in the Doppler beams). The laser was locked to Feature (a) of Line # 954 of iodine [101], which is shown in Fig. 4.4(b). Thus, the complete frequency offset between

Table 4.2: Optical characteristics of rubidium dihydrogen phosphate (RDP) at 626 nm and room temperature [104]. The second-harmonic generation scheme uses Type I phase-matching: 626 nm (ordinary ray) + 626 nm (extraordinary ray) = 313.0 nm (extraordinary ray).

property	value
refractive index (o,e)	1.51, 1.49
$d_{eff}$	0.379 pm/V
walk off angle (o,o,e)	0 mrad, 0 mrad, 3.02 mrad

the iodine frequency  $\nu_{I_2}$  and the frequency  $\nu_r$  of the repumper light at the ion satisfied

$$\begin{aligned}
 \nu_r &= 2\nu_{I_2} + 2 \times 661 \text{ MHz} + 2 \times \frac{1}{2}\nu'_{mod} + 80 \text{ MHz} \\
 &= 2\nu_{I_2} + 1362 \text{ MHz}.
 \end{aligned}
 \tag{4.4}$$

The 626 nm light in the repumper beam line was doubled by single-passing it through an rubidium dihydrogen phosphate (RDP) crystal. The relevant optical characteristics of RDP are at 626 nm are shown in Table 4.2. The crystal was 5 cm long, and was cooled (using a thermoelectric cooler) to  $-1.86^\circ\text{C}$  for  $90^\circ$  (non-critical) Type I phase matching. The red light was focussed into the crystal with a 10 cm focal length lens. With 200 mW of power at 626 nm, the crystal produced  $\approx 17 \mu\text{W}$  of 313 nm UV light, which corresponds to  $\eta_{nl} \approx 3.5 \times 10^{-4}/\text{W}$ . As indicated in Fig. 4.2, the UV passed through a +80 MHz switch AOM, before being combined with the Red and Blue Doppler beams on a 50-50 beam splitter and passing into the trap.

#### 4.1.2 The Raman Beam Line

The Raman beams were produced by another home-built ring dye laser, of the same design as that which produced the repumper light. This laser was locked to an external Invar cavity similar to that in the repumper setup, which provided frequency stability. Since stimulated-Raman transitions were used to couple the ion's spin and motion (see Ch. 3), the overall laser frequency stability was not as important as that

of the frequency difference of the two Raman beams. This difference frequency was set by a high-frequency AOM (driven at 550 MHz) through which the Raman light passed before being coupled into two single-mode fibres and over to the UV table (see Fig. 4.6). Drifts in the overall Raman laser frequency produced only higher-order effects in the laser coupling to the ion: from Eq. (3.27),

$$\begin{aligned}\delta\Omega &= \frac{g_2^* g_1}{\Delta_R^2} \delta\Delta_R \\ \Rightarrow \frac{\delta\Omega}{\Omega} &= \frac{\delta\Delta_R}{\Delta_R},\end{aligned}\tag{4.5}$$

where  $\delta\Delta_R$  is the fluctuation in the Raman laser detuning. For this reason, it was not necessary to stabilize the laser to a narrower linewidth than the 50–100 kHz it exhibited when locked to the external Invar cavity. Nor was it necessary to lock the Raman laser to an iodine feature for long-term stability.<sup>8</sup>

Once the 626 nm light passed through the optical fibres to the UV table, it was coupled into a two-ring buildup cavity of the same design as that in the Doppler beam lines. The 626 nm light was doubled in BBO. The design parameters and the doubling efficiency of this setup were the same as with the Doppler beam rings.

From the doubling ring, the Blue Raman (which was detuned by  $\Delta_R$  from the  $|\downarrow\rangle \leftrightarrow |v\rangle$  transition) beam passed through a noise-eater detector and AOM setup identical to that in the Blue Doppler beam line. The undeflected beam from the noise-eater AOM (which had reduced amplitude fluctuations) then passed through a switch AOM driven at 80 MHz: the negative first-order beam was selected for use in the experiment. This beam was combined with the Red Raman (detuned by  $\Delta_R$  from the  $|\uparrow\rangle \leftrightarrow |v\rangle$  transition) co-propagating beam on a polarizing beamsplitting cube, and then focussed onto the ion by a 10 cm focal length lens, which was mounted on an XYZ-translation stage.

---

<sup>8</sup> The Raman laser typically exhibited a drift rate of  $\approx 200$  MHz/h.

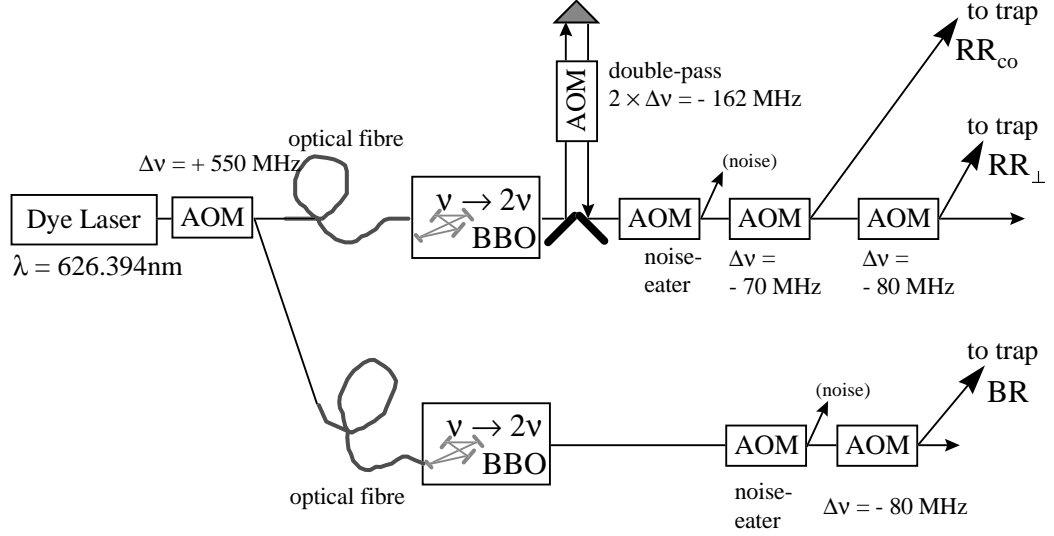


Figure 4.6: Raman beam line. The Red and Blue Raman beams were split in the red, then sent to the UV table through optical fibres. Blue Raman was detuned by  $\Delta_R$  from the  $|\downarrow\rangle \leftrightarrow |v\rangle$  transition, while Red Raman was detuned from the  $|\uparrow\rangle \leftrightarrow |v\rangle$  transition. Since we used Raman transitions to couple spin and motion, frequency fluctuations of the laser were not significant to first order. For this reason, no  $I_2$  lock was needed. The double-pass AOM in the Red Raman beam line determined the overall frequency separation of the Red and Blue beams: the double-pass configuration allowed us to scan the frequency over a large (30 MHz) range without introducing appreciable beam steering.

The Red Raman UV beam line was somewhat more complicated. This beam had the frequency-control elements in it. It was also split into two, independent beam lines: the co-propagating<sup>9</sup> ( $RR_{co}$ ) and the perpendicular ( $RR_{\perp}$ ) beams. From the doubling ring, the Red Raman UV beam went to a double-pass AOM which set the overall difference frequency between the Blue and Red Raman beam lines. The rf which drove this AOM came from a switchable rf multiplexer, which could switch one of many different rf sources to the AOMs rf input. By selecting the frequencies of these rf sources appropriately, we could drive any of the interesting ion-laser couplings (see Ch. 3): carrier, blue sideband, red sideband, etc. Usually, a frequency of approximately 80 MHz

<sup>9</sup> This beam, in conjunction with the Blue Raman beam, drove transitions for which  $\Delta\mathbf{k} \approx 0$ , which were insensitive to the ion's motion (see Sec. 3.3).

sent to the double-pass AOM drove the carrier transition (90° configuration): this frequency corrected for Zeeman shifts of the atomic levels due to the applied quantization magnetic field (see above). The details of the rf switching will be discussed in Sec. 4.2.1. The double-pass configuration of the AOM allowed us to change the frequency of the Red Raman beam by a large amount (up to 30 MHz) without appreciable beam steering.

After the double-pass AOM, the beam passed through a noise-eater AOM setup similar to those in the Blue Doppler and Blue Raman beam lines. Since the noise-eater was downstream of the double-pass AOM, it could correct for imbalances in the rf levels of the various synthesizers which drove the double-pass.

Having passed through the noise-eater AOM, the Red Raman beam continued on through an AOM which split the perpendicular and co-propagating Red Raman beams. This AOM was driven with 80 MHz rf, and the negative, first-order deflected beam was combined on a polarizing beamsplitting cube with the Blue Raman beam (see above). This beam constituted the co-propagating (“...with the Blue Raman”) beam, and could be switched off by turning off the rf driving the “splitter” AOM. The undeflected beam from the splitter AOM passed into a final AOM (the “Red Raman switch”) driven with 80 MHz rf, and the negative, first-order deflected beam passed through a 10 cm focal-length lens (mounted on an XYZ-translation stage) and into the trap.

From Fig. 4.6, we may determine the frequency differences between the  $RR_{co}$  and  $BR$  beams, and between the  $RR_{co}$  and  $RR_{\perp}$  beams at the ion. These are:

$$\begin{aligned} \Delta\nu_{BR,RR} &= 2 \times 550 \text{ MHz} - 80 \text{ MHz} + 2\nu_{dp} + 80 \text{ MHz} \\ &\approx 1100 \text{ MHz} - 80 \text{ MHz} + 2 \times 81 \text{ MHz} + 80 \text{ MHz} \\ &= 1262 \text{ MHz} , \end{aligned} \tag{4.6}$$

$$\Delta\nu_{co,\perp} = -80 \text{ MHz} + \nu_{splt} . \tag{4.7}$$

In Eq. (4.6),  $\nu_{dp}$  is the frequency driving the double-pass AOM: for the last equality, I have assumed that this frequency was set to drive the carrier transition. In Eq. (4.7),

$\nu_{splt}$  is the frequency driving the splitter AOM: had this frequency been set to 80 MHz, then the two carrier transitions (perpendicular and co-propagating) would have been at the same double-pass frequency. In practice, the frequency was usually set to  $80 \text{ MHz} - \omega_m/2\pi$  so as to allow coherent-state generation (see Sec. 6.1.3), so that the two carrier transitions did not correspond to the same double-pass AOM frequency.

#### 4.1.3 Revisions to the Laser Beam Lines

The optical setup described above held for many of the experiments described in this thesis. However, two major changes were made to this setup in the spring of 1998. One involved the resonant beams, and the other involved the Raman beams.

The Coherent 699 laser used to produce the Doppler beams frequently exhibited a linewidth of  $\approx 4 \text{ MHz}$  at 626 nm. This translated into a spectral width of  $\approx 8 \text{ MHz}$  in the UV — a substantial fraction of the  ${}^9\text{Be}^+$  excited-state linewidth. The laser noise produced a widening of the normally Poissonian photon distributions of the cycling transitions (see Sec. 3.1). Since the homemade lasers had much narrower linewidths, we decided to use what had formerly been the repumper dye laser to drive the cycling transition, and the 699 as a repumper. However, we continued to use the 699 to produce the Red Doppler beam. This necessitated changing the Red Doppler transition from being resonant with the  $|\uparrow\rangle \rightarrow |2p^2P_{3/2}\rangle$  transition to being resonant with the  $|\uparrow\rangle \rightarrow |2p^2P_{1/2}\rangle$  transition. However, this was a minor change. This switch in laser roles had the desired effect on the photon statistics.

A second major change was prompted by the discovery that the single-mode fibres used to translate the Red and Blue Raman beams from the red table to the UV table introduced significant phase noise between the two beams. This problem was resolved by the purchase of several 250 MHz UV AOMS, which enabled the  $\approx 1.25 \text{ GHz}$  hyperfine splitting between the Red and Blue Raman beams to be achieved in the UV. In the new scheme, the 626 nm light was transported to the UV table with a single fibre, and then

doubled. The double-pass AOM frequency was changed slightly, but the Red Raman splitter and the Red Raman switch frequencies were kept the same. A high-frequency AOM was placed upstream of the double-pass AOM and driven at 257 MHz. Its positive, first-order diffracted beam was then passed through three other AOMs, all driven at 257 MHz. In each case, the positive, first-order beam was passed on to the next AOM, and the resulting beam was taken as the Blue Raman, with the last high-frequency AOM being used as the new Blue Raman switch.<sup>10</sup> The total frequency separation of the Red and Blue Raman beams at the trap was thus given by

$$\begin{aligned}
 \Delta\nu_{tot} &= 4 \times 257 \text{ MHz} + 2 \times \nu_{dp} + 80 \text{ MHz} \\
 &\approx (1028 + 2 \times 77 + 80) \text{ MHz} \\
 &= 1262 \text{ MHz} = \omega_0/2\pi .
 \end{aligned}
 \tag{4.8}$$

A schematic of the modified Raman beam line is shown in Fig. 4.7.

#### 4.1.4 Photon Detection

Fluorescence from the ion was collected by an  $f/1$  optical system, the details of which are shown in Fig. 4.8. This system consisted of two lenses, with an aperture between the two.

The first lens was a six-element compound lens (designed by Howard Smith and assembled by Coastal Optics), with a working distance of 40 mm. A 600  $\mu\text{m}$  diameter aperture was located at the position of the primary focus. After passing through this aperture, the collected fluorescence was focussed by a second lens (a 2.5 cm focal length, Newport UV doublet consisting of two, 5 cm lenses) onto either one of two photon counting devices (see below). The magnification of the first lens assembly was 5 and that of the second was 25, for an overall magnification of 125.

---

<sup>10</sup> The higher frequency operation had the added benefit of increasing the angular separation of the different diffracted orders, making it easier to separate the desired order from the others and reducing stray light

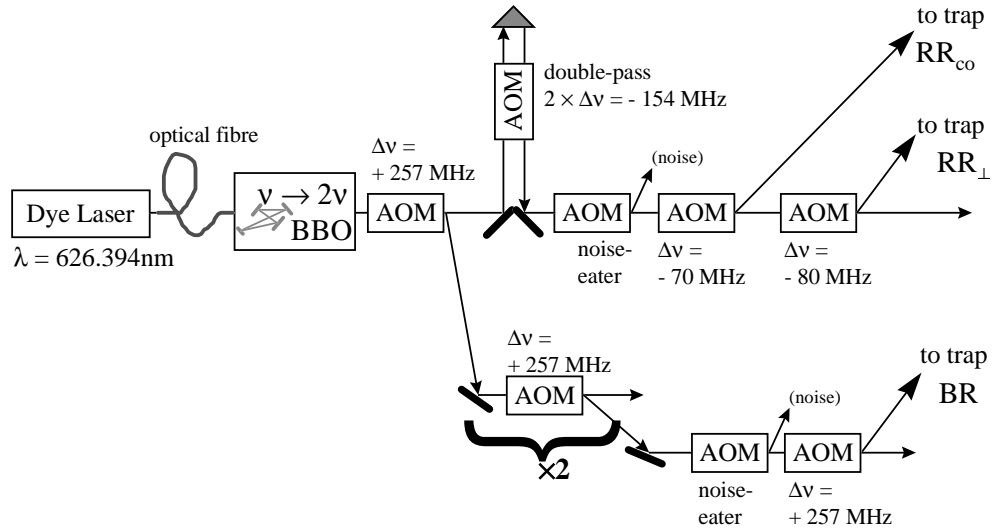


Figure 4.7: Raman beam line as modified to avoid fibre-induced, differential phase noise in the Red and Blue Raman beams. The 626 nm light now passed to the UV table through a single fibre, and was frequency doubled to 313 nm before being split. The Red Raman beam line was identical to before (see Fig. 4.6). The Blue Raman beam passed through four, 257 MHz AOMs in order to pick up a frequency shift with respect to Red Raman equal to the hyperfine splitting plus Zeeman shifts.

The fluorescence was either imaged onto a micro-channel plate imaging tube or a photomultiplier tube (PMT). The former was convenient for forming an image of the trapped ion and its environs, but had lower quantum efficiency than the photomultiplier tube. For this reason, the imager was used for loading the trap, but the PMT was usually used for taking data.

Two imager tube systems were used in the experiments described in this thesis. The first was manufactured by Quantar Technologies. It had a quantum efficiency of  $\approx 5\%$ . The second was produced by Photek, and had roughly the same quantum efficiency. Both tubes produced voltage outputs proportional to the  $x - y$  position of the detected photons: these outputs could be displayed on an oscilloscope, producing a real time image of the fluorescing ion. In addition, both tubes had digital outputs which allowed an integrated picture to be displayed on a computer. The inset of Fig. 2.2 shows

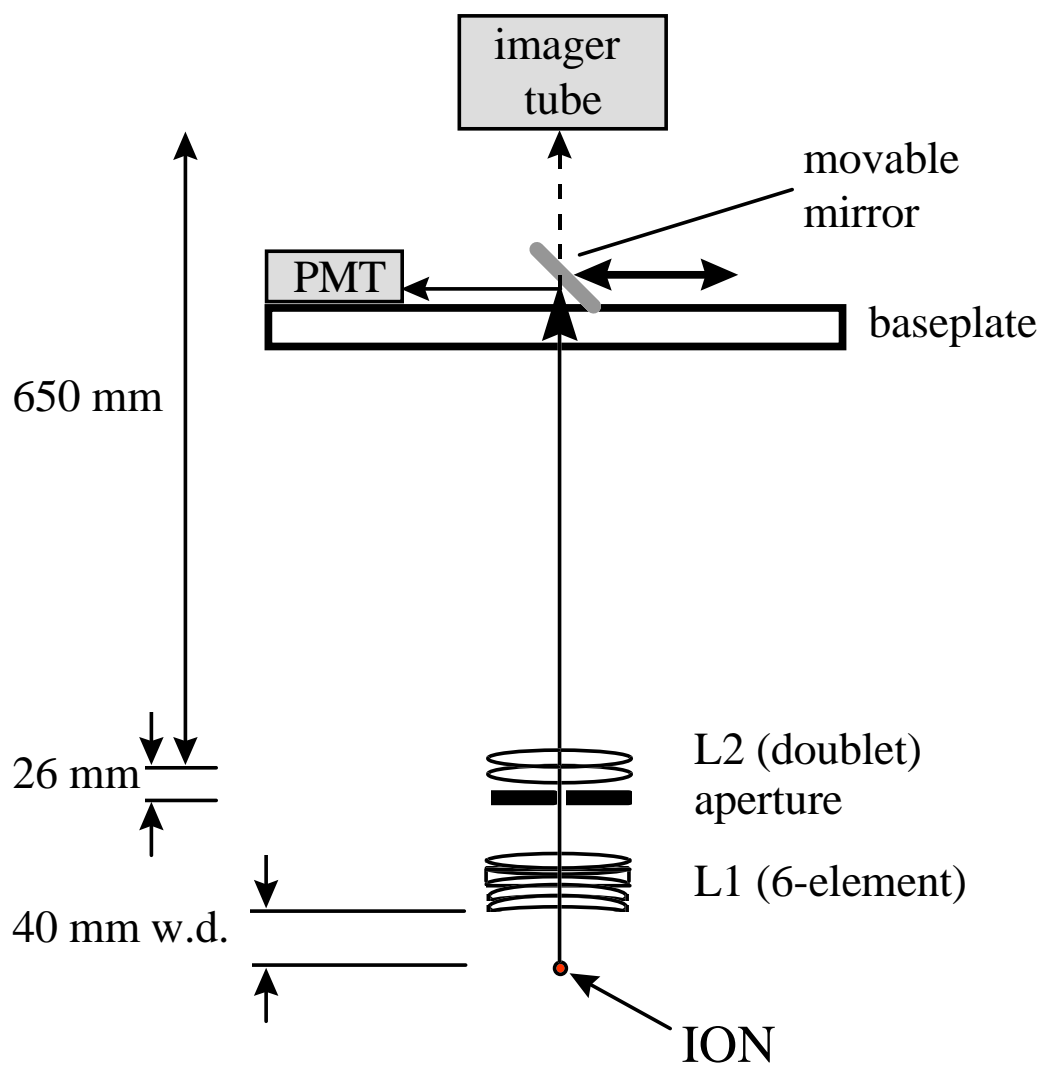


Figure 4.8: Schematic of the imaging optics. The first lens was a custom-made (Howard Smith, design/Coastal Optics, assembly) six-element lens with a working distance of 40 mm. The second was a 2.5 cm focal length Newport UV doublet. The overall magnification of the system was 125, and its  $f/\#$  was equal to one.

an image of two trapped ions held in the beryllium-electrode elliptical microtrap. These data were taken with the Photek imager. Finally, both imaging tubes output a TTL-compatible pulse for every photon they detected. These pulses could then be counted by the data-acquisition system (see Sec. 4.2.2), or converted to an average count rate. The photomultiplier tube was a Hamamatsu Model #H6240-01 “side-on” PMT. Its quantum efficiency was  $\approx 20\%$ . This unit takes +5 V in and puts out a TTL-compatible pulse for every photon it detects.

The imager tube (whichever one was in use) and the photomultiplier tube were mounted on the base plate (see Fig. 4.8). The imager was mounted facing the ion and the PMT at right angles. The fluorescence was usually focussed directly onto the imager photo-anode. However, by putting a  $45^\circ$  mirror into the path of the fluorescence, the light could instead be diverted onto the PMT’s window. This mirror was mounted on a motorized stage, and the whole assembly was made light-tight.

When counting photons with the photomultiplier tube, the overall detection efficiency of the system was calculated from the measured ion fluorescence to be  $\approx 8 \times 10^{-3}$ , when it was used with the linear trap. The detection efficiency includes effects due to the ion’s dipole radiation pattern, the solid angle of the detection system, losses in the optics, and the quantum efficiency of the PMT. Due to said dipole radiation pattern, the detection efficiency with the elliptical traps was two-thirds this value (since these traps were viewed at  $90^\circ$  to the plane of the laser beams).

## 4.2 Experiment Control and Data Acquisition

Before delving into the details of the control logic for the experiment, or into the details of the photon-counting, it will be worthwhile to provide an overview of how the experiment ran. Each single experiment generically consisted of four parts: (1) laser cooling (Ch. 5) and optical pumping to  $|\downarrow, n=0\rangle$ , (2) quantum state engineering (Chs. 6 through 9), (3) mapping motional information onto the spin (Sec. 3.5), and (4)

measuring fluorescence on the cycling transition (Sec. 3.1 and Appendix A). Of course, sometimes certain of these parts were absent, or mingled together: as an example, in creating Schrödinger cat states (see Sec. 6.2.1), the state engineering was actually sandwiched between two parts of the motion/spin mapping.

In taking data, the experiment was usually repeated many times while some parameter was changed. To be more concrete, let us assume that the particular experiment at hand consists of creating some motional state and then taking a Rabi flopping curve (Sec. 3.2) on the blue sideband. To acquire such a curve, we would change the parameter  $t_{pr}$ : the length of the blue sideband “probe” pulse. At each value of  $t_{pr}$ , we would, in principle, repeat the experiment enough times to obtain good signal-to-noise on the probability  $P_{\downarrow}$  that the atom is in  $|\downarrow\rangle$  after the probe pulse. In actuality, the dwell time was chosen to make the settling time of the pulse-producing instrument negligible with respect to the dwell time. Typically, about one hundred experiments were taken at each value of  $t_{pr}$ . By repeating this procedure for  $t_{pr}$  ranging from zero to  $t_{max}$ , we would obtain a curve such as Fig. 3.4(b).

A typical experiment took about one millisecond to execute, so that each data point took about one-tenth of a second. Thus, for example, the entire Rabi flopping curves of Fig. 3.4 took about 20 s to obtain.

The experiment thus consisted of two time scales: a fast time scale on which, in the course of a single shot, the various laser beam combinations needed for cooling, state creation, and mapping were turned on and off, and a slower time scale on which (every ten to one thousand repetitions of the single shots), parameters such as the length or frequency of the probe pulses were changed. This latter time scale was the time scale on which the data acquisition took place. I shall describe this in Sec. 4.2.2. First, however, I shall discuss the laser beam switching.

### 4.2.1 Switching Logic

A diagram showing the control aspects of a single experiment is shown in Fig. 4.9. As this diagram indicates, it was necessary not only to switch laser beams on and off in various combinations, but also to change the frequency of the Red Raman beam within the course of a single experiment. This change in frequency was accomplished by changing the frequency of the rf sent to the Red Raman double-pass AOM. The on/off switching for all the beams was accomplished by switching on and off the rf driving the various “switch” AOMs. Typical pulse lengths ranged from sub-microsecond (for a carrier transition) to hundreds of microseconds (for driving the cycling transition).<sup>11</sup>

The rf control (both on/off and frequency) was accomplished through a large rf “switchbox.” The heart of this box were the Mini-Circuits ZYSWA and GSWA, TTL-controlled rf switches. The ZYSWA switch has two rf inputs and one rf output (although the switch could also equally well work in reverse configuration with one input and two outputs). A TTL input controlled which of the two rf inputs was connected to the output. If only one rf input was connected to an rf source, the switch functioned as a TTL-controlled on/off switch. If both inputs were connected to rf sources, the switch acted as a multiplexer. The TTL inputs floated high (logic 1). The GSWA is a four input version of the ZYSWA and, for our use, four of these were wired up as a 16- input multiplexer, controlled by four TTL lines.

The rf portion of the rf switchbox contained the 4-bit, 16-input multiplexer, two 2-bit, 4-input multiplexers, and seven (one-input) on/off switches. The box also contained some TTL logic, which I will discuss below. A schematic of these parts of the rf switchbox is shown in Fig. 4.10(a).

---

<sup>11</sup> Of course, these values are meant to be representative. The actual pulse lengths were determined by the relevant Rabi frequencies, which depended on the laser power, beam waist at the ion, Raman laser detuning from the  $2p \ ^2P_{1/2}$  level, etc. These factors varied from day to day and from week to week. However, this variation was rarely more than a factor of two.

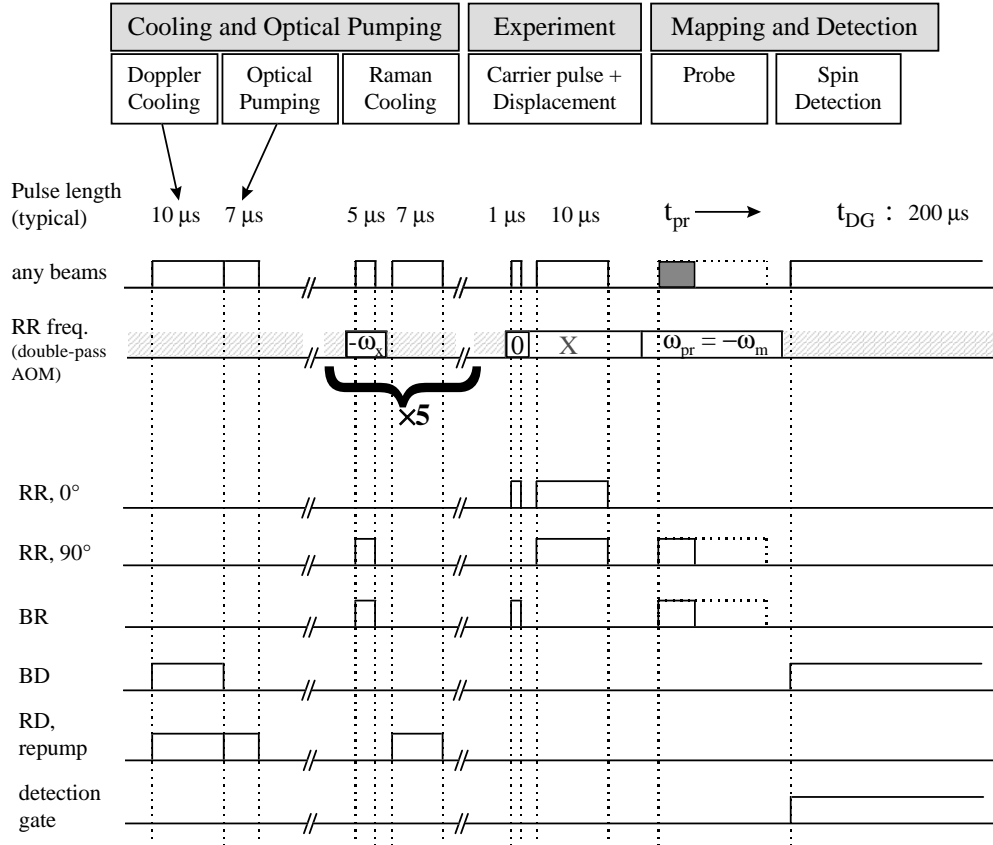


Figure 4.9: Timing diagram for a typical experiment. In this experiment, a coherent state (Sec. 6.1.3) is created in  $\uparrow$ , then a Rabi flopping curve is taken on the red sideband. The experiment consists of (1) Doppler cooling (2) optical pumping to  $|\downarrow\rangle$  by Red Doppler and the repumper (3) Raman cooling (4) a  $\pi$ -pulse on the co-propagating carrier to flip the spin (5) a  $10 \mu$ s coherent displacement pulse on the two Red Raman beams (“walking standing wave”) (6) a probe pulse on the red sideband for variable time  $t_{pr}$  (7) detection of  $P_{\downarrow}(t_{pr})$  by driving the cycling transition with Blue Doppler. The indicated pulse lengths are typical values.

The 16 input multiplexer controlled the rf signal source which was sent to the Red Raman double-pass AOM. Each frequency of interest (i.e. corresponding to the blue sideband, the red sideband, the co-propagating or perpendicular carrier, etc.) was derived from a separate rf synthesizer, and this rf source was selected at the appropriate point in the experiment. We typically used either Fluke Model #6160B or HP Model #3335A synthesizers. The “probe” frequency, however, had to be swept when we

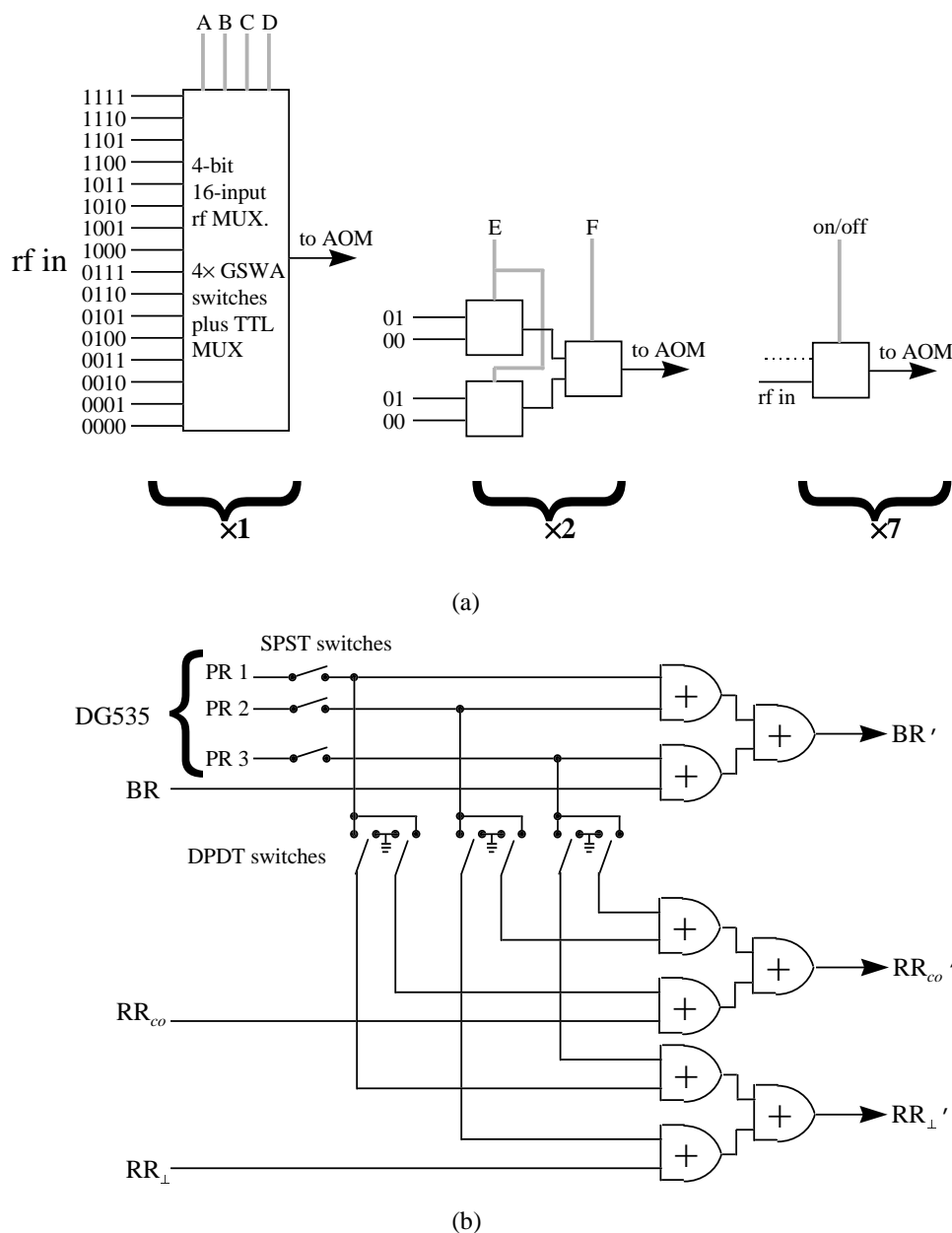


Figure 4.10: (a) Schematic of the rf portion of the "rf switchbox" circuitry. The individual rf switches were Mini-Circuits ZYSWA, TTL-controlled rf switches. These either operated as on/off switches, or were cascaded together to make rf multiplexers. The box contained one 4-bit, 16-input multiplexer, two 2-bit, 4-input multiplexers, and seven rf on/off switches. (b) Schematic of the TTL circuitry inside the "rf switchbox." This circuitry performed a logical OR operation between the BR, RR, and/or Co outputs of the HP 8175 and the output of the Stanford Research DG535 "probe" pulse generator.

wished to take spectra. The rf source for this pulse was a GPIB-controlled HP Model #8660D. The GPIB interface was fast enough to allow the frequency to change in a few milliseconds, as will be discussed in Sec. 4.2.2. All the rf synthesizers driving the UV AOMs were phase-locked together.

One of the two 4-input multiplexers was used to switch in different rf sources to the Red Raman splitter AOM, which separated the co-propagating from the perpendicular Red Raman beams. These two beams were turned on simultaneously to create coherent or squeezed states using the “walking standing wave” technique (see Sec. 6.1.3), and the multiplexer allowed us to switch rf of different phases to the splitter AOM, thus putting different relative phase shifts between the co-propagating and perpendicular Red Raman beams. Note that the rf could also be turned off by not connecting one of the inputs to an rf source, and selecting that vacant input when the co-propagating Red Raman beam was wished to be off.

The other 4-input multiplexer was usually left unused. It was, however, used for creating coherent states (Sec. 6.1.3) by driving the trap electrodes with electric fields (oscillating at the trap frequency) — again, the multiplexer allowed us to switch in rf of different phases. It was also used in trying the Sørensen and Mølmer scheme for creating maximally entangled states (Sec. 6.4.2).

The TTL control pulses which turned the rf switches on and off and selected the rf multiplexer inputs were produced by an HP Model #8175 digital pulse generator. This instrument has up to 24 TTL output channels. By setting the appropriate control bits, any combination of the outputs can be set to logic 0 or 1 (0 or  $\approx 5$  V). The 8175 scans through its memory one 24-bit word at a time, and sets the appropriate TTL values on its outputs. The length of time spent at each 24-bit word is programmable: it may be any length of time from 20 ns to one second. This allows one to efficiently output a pulse sequence even if it contains pulses of widely varying lengths (for example, a carrier  $\pi$ -pulse versus driving the cycling transition). The repetition rate at which the HP 8175

repeated its scan through its memory was set by a Stanford Research Model #DG535 digital pulse generator: each pulse from the DG535 triggered one scan through the HP 8175's memory. The frequency of the pulses from the DG535 was set to be the inverse of the sum total of the pulse lengths in a single shot of the experiment.<sup>12</sup>

The HP 8175 output the four control bits for the 16-input multiplexer and the four control bits for the two 4-input multiplexers. It also output the on/off signals for the Red Doppler (RD) (which also controlled the repumper switch), Blue Doppler (BD), the Blue Raman (BR), Red Raman perpendicular (RR), and Red Raman co-propagating (Co) beams. However, the HP 8175 output for these latter beams was logically OR-ed with the output of a second Stanford DG535 pulse generator, as will be discussed below. The HP 8175 also put out the TTL-logic Detection Gate (DG) pulse, which determined when photons detected by the imager tube or the photomultiplier tube were counted by the data acquisition systems. Finally, it put out trigger signals for the "probe" DG535 and trigger signals which could be used to change the trap voltages (to change the trap frequency or to move ions around in the trap).

In the course of taking data, it was desirable to be able to quickly change the length of the probe pulse. This probe pulse consisted of either Blue and Red Raman, or Blue Raman and the co-propagating Red Raman beam. As discussed in the introduction to this section, this probe length had to be changed every ten to hundred milliseconds. The GPIB interface for the HP 8175 was far too slow to allow this. For this reason, and to allow differing configurations of the probe pulse, the probe pulse was created by the second DG535 pulse generator, which was triggered by the HP 8175 at the appropriate point in each experiment. This pulse was then logically OR-ed with the Blue Raman (BR) 8175 output and either the Red Raman (RR) or co-propagating Red Raman (Co) output. The circuitry to do this was housed inside the rf switchbox, and is shown

---

<sup>12</sup> with some extra time added in for a margin of error

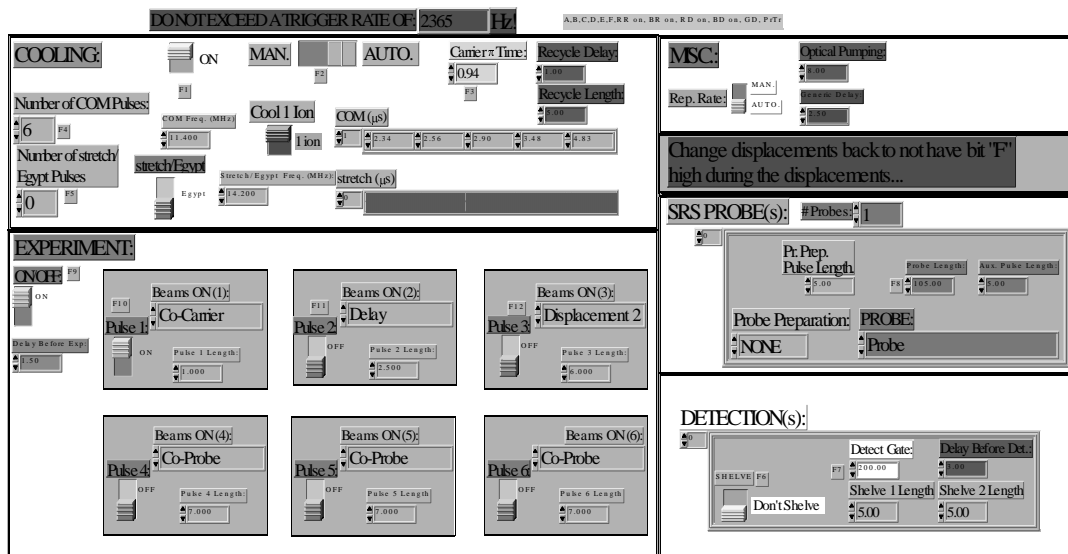


Figure 4.11: User interface for the LabView program which set up the HP 8175 pulse generator to run the experiment. This program offered the user a convenient, menu-like means of selecting which laser beams to turn on, then converted this information to ASCII arrays of “which beams” and pulse length information, then downloaded these arrays to the HP 8175.

in Fig. 4.10(b). The length of the probe pulse was controlled by the data acquisition programs (see Sec. 4.2.2).

The GPIB control of the HP 8175 was accomplished through a LabView program running on a PC. This program offered a convenient user interface, which allowed us to select pulse combinations and pulse lengths in a menu-like format. The user interface to the program is shown in Fig. 4.11. Once the desired sequence of pulses was selected, the program produced an array of pulse lengths and a corresponding array of “which beam is on” information, and transmitted these arrays in ASCII format to the HP 8175 according to the IEEE 488.2 (GPIB) interface standard.

## 4.2.2 Data Acquisition

As mentioned in the introduction to this section, the data acquisition occurred on a slower time scale than that of a single experiment. Nonetheless, the data acquisition

equipment had to take in photon counts every experiment — that is to say, every millisecond — and change the probe pulse length, phase, or frequency every ten to hundred experiments. These timing requirements were too stringent to allow control by, say, a PC, and less straightforward methods were required.

Much of the data were taken on HP Model #9826 computers. These computers, which dated from the early 1980's, were old, but dated from a time when the microprocessors were “weighted down” by far fewer interrupts than those in modern PC's. When running the FORTH operating system/programming language, they were able to identify and service an experiment-generated flag in as little as tens of nanoseconds. Thus, they were more than adequate for our needs. The programs for these computers were written and maintained by Wayne Itano.

In their data-taking role, these computers worked with a home-built counter/buffer box. This box took in photon counts (which were logically AND-ed with the Detection Gate pulse from the HP 8175), and stored them in a buffer until the computer could process the data. A schematic of this counter/buffer box is shown in Fig. 4.12. The computer processed the data and updated the probe time, phase, or frequency by communicating with the appropriate device — Stanford Research DG535, HP 3335A, or HP 8660D, respectively — over the GPIB bus.

The programs used to take much of the data actually ran *asynchronously* with the experiment.<sup>13</sup> A separate clock set the rate at which the counter/buffer box accepted counts and passed them onto the computer, and also the rate at which the computer updated the instruments over the GPIB bus. The clock rate was set by hand to be roughly ten times (for spectra) or one hundred times (for flopping curves)<sup>14</sup> the experiment repetition rate. Although this meant that the exact number of experiments

---

<sup>13</sup> Synchronous versions of these programs were created, but the desire for familiarity led to continued use of the original program versions.

<sup>14</sup> The HP 8660D executed GPIB updates much more quickly than the DG535, and settled to its new parameter values faster. For this reason, the spectrum program could spend less time at each data point than the flopping program, as there was a smaller time period during which the parameter values were ambiguous.

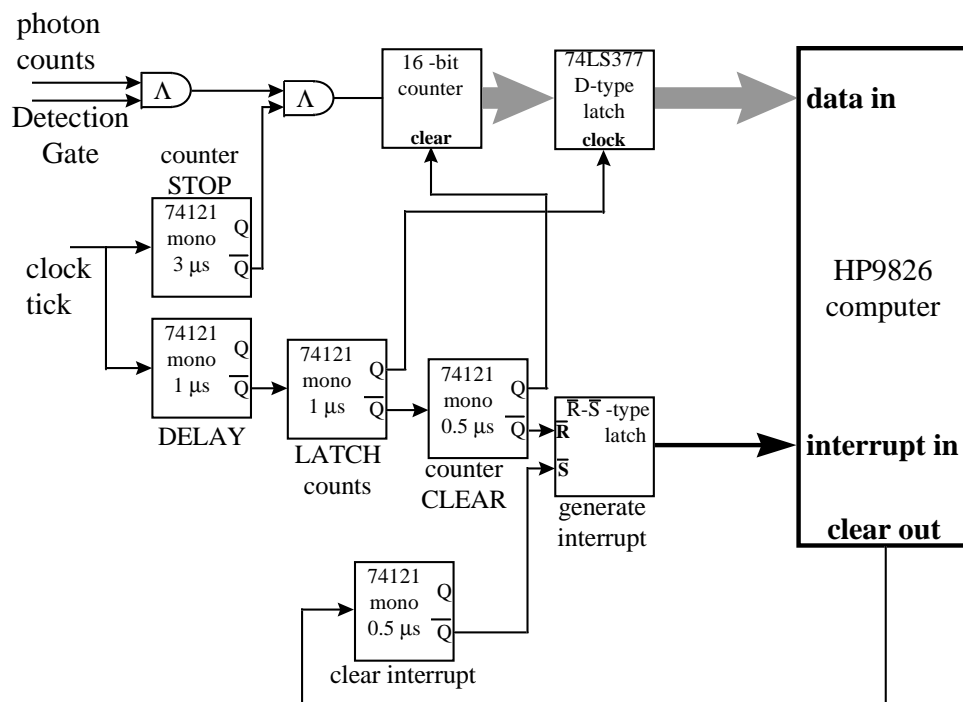


Figure 4.12: Schematic of counter/buffer box for data acquisition with HP 9826 computers. Upon receiving a clock tick, the “counter STOP” one-shot outputs a logic “low” which stops the counting. The value of the counter is then latched into the data latch, after which, the counter is cleared, and an interrupt for the HP 9826 is generated. The HP 9826 then reads the latched data, processes it, then clears the interrupt. The photon counts are “ANDed” with Detection Gate before passing on to the counter.

per data point differed at different data points (by perhaps one experiment), this was not significant. The same could be said for the settling time of the instruments after the GPIB update command received: this effect merely amounted to a smoothing of the data. In any case, the programs were carefully evaluated, and these effects were not found to be appreciable.

As alluded to above, there were three main types of programs run on the HP 9826 computers. The first was a spectrum-taking program, which changed the frequency of the probe HP 8660D synthesizer. Typically, each data bin was 10 ms long when using this program (although this was changeable), so that each data point consisted of about

ten experiments. The second type of program used was one which changed the length of the pulse put out by the probe DG535 pulse generator in order to take Rabi flopping curves. For this program, the dwell time was usually 100 ms per data point, or on the order of a hundred experiments. Finally, we used a third type of program to sweep the phase of the rf put out by one of the HP 3335AA synthesizers driving the Red Raman splitter AOM. This program was useful for taking Ramsey spectra, but was mostly used in the Schödinger cat experiments (see Sec. 6.2.1) and for density-matrix reconstruction (see Sec. 6.3). The dwell time with this program was also 100 ms per data point.

Various varieties of these programs were used at different times. Most of these were minor variations on the basic programs. However, it is worthwhile as an example to single out the program used to perform density-matrix reconstruction of the ion's motional state. As will be discussed in Sec. 6.3, this required us to displace the motional wave packet in various directions in the  $z-p$  plane. This was done by applying different rf phases to the Red Raman splitter AOM. For each phase, the probabilities  $P_n$  that the ion was in the motional Fock state  $|n\rangle$  had to be determined from blue sideband Rabi flopping curves. The data acquisition program for this experiment thus had two control loops. The inner loop changed the probe DG535 pulse length to obtain a Rabi flopping curve at each phase of the HP 3335A. Once a flopping curve was completed, the outer control loop then changed the phase of the HP 3335A.

As discussed at the beginning of this section, it was not straightforward to implement similar programs on a PC. Due to calls by different interrupts at different times, a PC cannot be trusted to execute data-acquisition code at sub-millisecond to millisecond timescales in a deterministic fashion. Nonetheless, it was possible to create programs which used plug-in data acquisition cards. These programs could not acquire data at the sub-millisecond level (as the HP 9826's could), but could reliably acquire data with only a few (2 to 5) milliseconds dead time in between acquiring one data point's data and being ready to receive the next point. The programs were thus suitable for our

experiments, and performed with no noticeable increase in experiment dead time. The programs were written in LabView.

The heart of these programs was a National Instruments PCI-MIO16E multi-function data acquisition board. This board featured two available “DAQ-STC” counter/timer chips, which allowed buffered counting. The photon counts from the imager tube or PMT were logically AND-ed with the Detection Gate pulse from the HP 8175, and sent to the input of one of the counters. Detection Gate also served as a clock to synchronize the counter’s acquisition of counts. These programs, therefore, were run *synchronously* with the experiment. The counters stored the number of photon counts at each Detection Gate “clock tick” into a different buffer location. Every few experiments, the PC was triggered to send a GPIB update to the appropriate instrument. The data at one instrument setting constituted one data point, as it had on the HP 9826 programs. Details of this set up are shown in Fig. 4.13.

On a longer timescale (usually two to four data points), the PC was triggered to read out the buffer, bin the data into the respective data points, average the data with corresponding previous data points, and update a graph with the new, averaged data.<sup>15</sup> Unfortunately, the AT-MIO-16E board could not generate a hardware interrupt from the counter chips. It was not possible, therefore, to simply count the number of Detection Gates received and send an interrupt to the PC after the appropriate number of experiments. However, the board did allow its analog input functions to generate interrupts upon completion of a channel scan. By using Detection Gate as the update clock of a “dummy” analog input scan, it was possible to achieve the desired effect.<sup>16</sup>

Each Detection Gate triggered the measurement of the voltage on an input of the D/A converter. At the end of one scan of the input channels, the D/A chip set a

---

<sup>15</sup> The graph update was the major bottleneck in the program. Unfortunately, it was not possible to run the graph update separately from the rest of the data acquisition program, due to LabView and Windows 95 OS constraints

<sup>16</sup> It was also possible to achieve the same end using an analog output scan — this could be convenient for experiments in which a trap electrode voltage is changed in the middle of an experiment

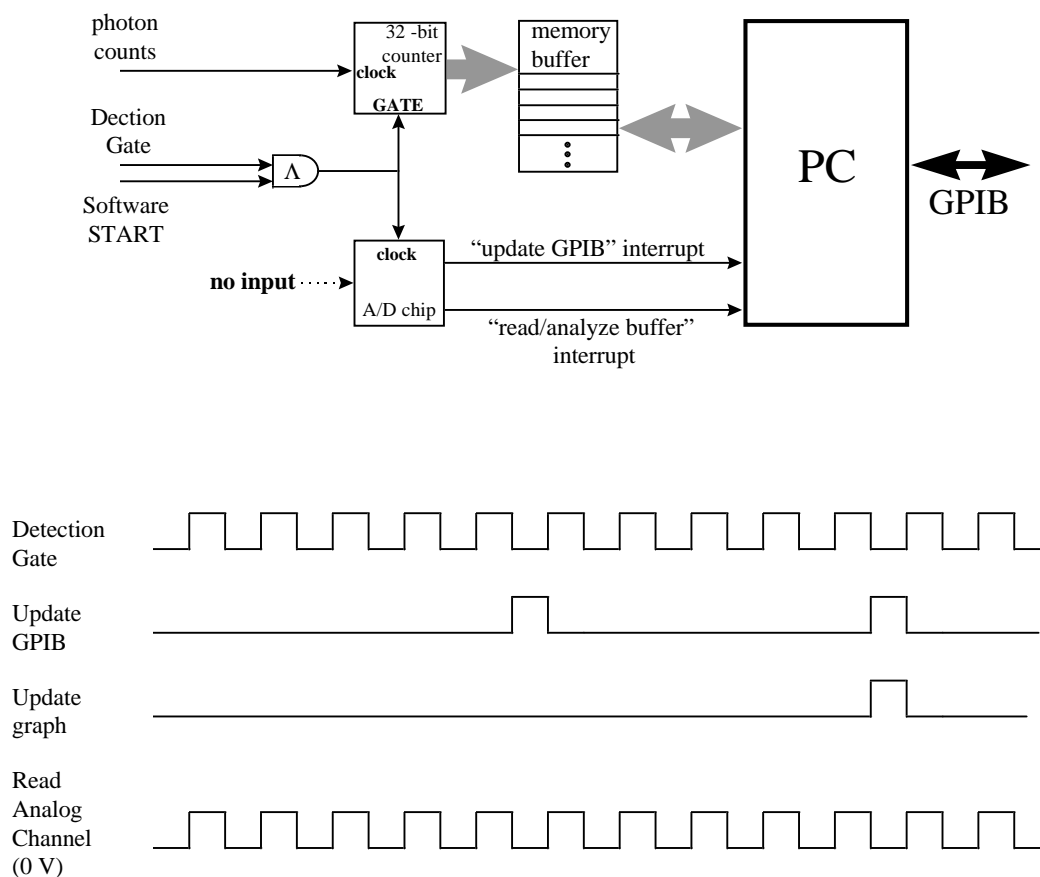


Figure 4.13: (a) Schematic of PC-based data acquisition system. Detection Gate serves both to gate the photon counts *and* as a data-acquisition clock. The counter latches its count value into memory every time its GATE (Detection Gate) goes low. In order to keep track of how many experiments have occurred, Detection Gate is used as the scan clock of a “dummy” analog input scan. This scan generated interrupts to tell the PC to update the probe instrument (DG535, HP 8660D, or HP 3335A) over the GPIB bus. On a longer time scale, the scan generated interrupts which caused the computer to read counts out from the counter’s memory buffer, analyze the data, and update its graphs. (b) Timing diagram for PC-based data acquisition. Detection Gate enables photon counting and serves as the scan clock for the “dummy” analog input scan. For this example, the probe instrument is updated every five experiments, and the data buffer is read and analyzed every ten experiments. In a typical experiment with a repetition rate of  $\approx 1.5$  kHz, the probe instrument was updated every 500 experiments, while the data buffer was read in every 1000 experiments.

hardware/software interrupt, which flagged the data acquisition software to change the probe instrument (DG 535, HP 8660D, or HP 3335A) settings over the GPIB bus. After several (usually two) such scans, another interrupt (similarly generated) triggered the buffer read out, etc. Details are shown in Fig. 4.13.

Programs were created on the PC which reproduced the HP 9826's spectrum, flopping, and phase programs with an efficiency appropriate for our data acquisition rates. In addition, a histogram-creating program was written which calculated and displayed a histogram of the number of photons received per experiment (typically, 1000 experiments were binned together for a single histogram update). As is discussed in Appendix A, this program was very convenient for peaking up the experiment.<sup>17</sup>

---

<sup>17</sup> Another diagnostic useful for peaking up the cycling transition was stand-alone Ortec Turbo MCS multi-channel analyzer. This instrument binned the photon counts according to their arrival time from the start of the Detection Gate.